Structural, electrical conductance and complex impedance analysis of (Nd1–xCex)0.7Sr0.3MnO3 (0≤x≤0.20) perovskite

Ridha Bellouz, Sami Kallel, Kamel Khirouni, Octavio Peña, Mohamed Oumezzine

Structural, Electrical conductance and complex impedance analysis of $(Nd_{1-x}Ce_x)_{0.7}Sr_{0.3}MnO_3$ ($0 \leq x \leq 0.20$) perovskite.

Ridha Bellouz [a], Sami Kallel [a], Kamel Khirouni [b], Octavio Pena [c], Mohamed Oumezzine [a]

[a] *Laboratoire de Physico-chimie des Matériaux, Département de Physique, Faculté des Sciences de Monastir,Université de Monastir, 5019, Tunisia.*

[b] *Laboratoire de physique des matériaux et des nanomatériaux appliquée à l'environnement, faculté des sciences de Gabes cité Erriadh, 6079 Gabes, Tunisia.*

[c] *Sciences Chimiques de Rennes, UMR6226-CNRS, Université de Rennes 1, 35042 Rennes Cedex, France.*

Abstract

Polycrystalline samples of $(Nd_{1-x}Ce_x)_{0.7}Sr_{0.3}MnO_3$ (x = 0, 0.10 and 0.20) were prepared by a high-temperature solid-state reaction technique. The X-ray diffraction study has shown that all the samples exhibit a single phase with orthorhombic structure (Space group Pnma). From the resistivity data, it is found that all the samples show metal to semiconductor transition and the transition temperature decreases with the Ce doping. The complex impedance has been investigated in the temperature range 80–320 K and in the frequency range 40 Hz–1 MHz. AC conductance analyses indicate that the conduction mechanism is strongly dependent on temperature and frequency. The impedance plane plot shows semicircle arcs at different temperatures and an electrical equivalent circuit has been proposed to explain the impedance results. The activation energies obtained from the conductance is slightly higher than that from time relaxation analyses.

Keywords: Perovskite, X-ray diffraction, Impedance spectroscopy, AC conductivity.

1. Introduction

The investigation of manganites with general formula $Ln_{1-x}A_xMnO_3$ (Ln=La, Nd, Pr, etc., A=Sr, Ca, Ba, etc.) has attracted extensive attention in the last decades due to its special physical properties and potential application. These manganite materials exhibit remarkable physical properties including colossal magnetoresistance (CMR), charge ordering [1, 2] and metal–insulator transition and also have potential applications for magnetic recording and magnetic sensors [**3,4**]. Most of the manganites presenting the CMR effect have a paramagnetic–ferromagnetic (PM–FM) transition at the Curie temperature. Their electrical resistivity shows a semiconductor behavior above T_C and a metallic behavior below T_C. The understanding of CMR phenomenon, metallic behavior and the strong FM interactions is generally based on the double exchange (DE) model [**5**]. In this model, there is an exchange of electrons from neighbouring Mn^{3+} to Mn^{4+} ions through oxygen when their core spins are parallel and hopping is not favoured when they are antiparallel. However, it was suggested that the DE model is not enough to explain the CMR phenomenon. Some authors suggested that other factors such as Jahn Teller effect [**6**] and phase separation [**7, 8**] are responsible for the behavior observed in manganite.

Several studies have been performed on the effect of substitution in the A-site by divalent elements (Sr, Ba…) [**9, 10**]. In fact, doping at the rare-earth site indirectly affects the conduction mechanism with its repercussion on bandwidth and bond angle between adjacent manganese ions [**11**]. The electrical conduction in these materials has contributions from grains (bulk), grain boundaries, and electrode specimen interface [**12, 13**]. In order to understand the conduction behavior, it is necessary to separate the various contributions to the total observed resistance. Complex impedance spectroscopy (CIS) is an important and powerful tool to study defects, microstructure, surface chemistry and electrical properties of materials. For a polycrystalline sample, this technique enables us to separate the contributions of bulk, grain boundary and electrode in the impedance very easily [**14, 15**].

Generally, $Nd_{0.7}Sr_{0.3}MnO_3$ perovskite undergoes a metal-semiconductor transition at the temperature T_{MS} of 229–239 K, [**17, 18**]. That is usually accompanied by a FM-PM transition at the Curie temperature T_C. It was shown by many authors that physical properties of $Nd_{1-x}Sr_xMnO_3$ can be considerably affected by the substitution of the Ln-site by various other elements such as Eu [19], La [20], Pr, Dy [21], Gd [22]. Recently, by doping Y ions into $Nd_{0.7}Sr_{0.3}MnO_3$, Khiem et al. [**23**] have found a decrease of T_C and a transition from a metallic phase to an insulating phase when the Y content increased. Padmavathi et al. [**24**]

have found that the transition temperature T_{MI} decreases with increasing $\langle r_A \rangle$ as Nd is progressively substituted by Ce in $Nd_{0.33}Sr_{0.33}MnO_3$.

The aim of this work is to study the structural and electrical properties (material impedance, electrical relaxation process, conductance behavior, etc.) of $(Nd_{1-x}Ce_x)_{0.7}Sr_{0.3}MnO_3$ ($0 \leq x \leq 0.20$) system using complex impedance spectroscopy (CIS) technique. The effects of temperature and frequency have been investigated and a pronounced contribution of the grain boundary in this compound is demonstrated.

2. Experimental procedures

Polycrystalline samples of $(Nd_{1-x}Ce_x)_{0.7}Sr_{0.3}MnO_3$ ($0 \leq x \leq 0.20$) have been prepared by conventional solid state reaction method. Stoichiometric ratio of Nd_2O_3, CeO_2, $SrCO_3$ and MnO_2 (previously dried at 800 K in order to remove any eventual water) were thoroughly mixed to get homogeneous powders, which were calcined at 1100 °C for 72 h. The calcined mixtures were then pressed into pellets (12 mm diameter and 2 mm thickness under 8 tons/cm^2) and sintered several times in air, with intermediate grindings, at 1400 K for 48 h. Finally, these pellets were quenched to room temperature. This step was carried out in order to preserve the crystalline structure at the annealing temperature. The structural characterization was done through X-ray diffraction measurements (XRD) using a ‘‘Panalytical X’Pert Pro’’ diffractometer with Cu K_α radiation (K_α=1.5406 Å). Data for the Rietveld refinement were collected in the range of 2θ from 10 to 100° at room temperature with a step size of 0.017° and a counting time of 18 s per step. The structure refinement was carried out by the Rietveld analysis of the powder XRD data with the FULLPROF software [**25**]. For the electrical measurements, the opposite sides of the sample were coated with conducting silver paint. The transport properties of the polycrystalline sample were examined by ac impedance spectroscopy using an Agilent 4294A over a frequency range from 40 Hz to 1 MHz at various steady temperatures (80–320 K). DC resistivity measurements were performed using the conventional four-probe method.

3. Results and discussion

3.1. Microstructure analysis

Fig. 1 shows typical XRD patterns performed at room temperature for x = 0.0 and 0.20 compounds. All samples were found to be single phase without any detectable impurity. There is no segregation of CeO_2 oxide as observed in many works [**24, 26**]. The structure refinement was performed in the orthorhombic setting of Pnma space group, in which the (Nd, Ce, Sr) atoms are at 4c (x, 0.25, z) position, Mn at 4b (0.5, 0, 0), O_1 at 4c (x, 0.25, z) and O_2 at 8d (x, y, z). We noticed that calculated diffraction patterns match well with measured ones. The difference observed between the intensities of the measured and calculated diffraction lines can be attributed to the existence of preferential orientation of the crystallites in the samples [**27**]. Positions for the Bragg reflection are marked by vertical bars. Differences between the observed and the calculated intensities are shown at the bottom of the diagram. The refinement results are listed in **Table 1**, which also reports the residuals for the weighted pattern R_{WP}, the pattern R_P, the structure factor R_F and the goodness of fit χ.

It is well known that the tolerance factor T_G **[28]** determines the crystal structure of ABO_3 perovskite. Only for T_G close to unity is a cubic perovskite structure obtained. For $T_G \neq 1$, a tilt and rotation of the oxygen octahedra are obtained compensating for the misfit of the ionic radiis of the involved A and B cations. This can be seen from the definition of T_G:

$$t_G = \frac{< r_A > + r_O}{\sqrt{2}(< r_B > + r_O)} \qquad \textbf{(1)}$$

Where r_A, r_B and r_O are respectively the average ionic radii of the A and B perovskite sites and oxygen anion. Usually, for ($0.96 \leq t_G \leq 1$), the connecting pattern of the oxygen octahedra is rhombohedral, whereas it can be orthorhombic or monoclinic for lower values of T_G. The values obtained of T_G (**see Table 1**) suggest that our samples have the orthorhombic phase with perovskite structure ($0.89 \leq t_G \leq 0.96$).

We can see in **Table 1** that the lattice parameters and unit cell volume increase slightly with increasing Ce content. This slight increase can be directly related to the increase of average ionic radius of A site $<r_A>$ which is due to the larger ionic radius of Ce^{3+} ion ($r_{Ce^{3+}}$ =1.196Å and $r_{Nd^{3+}}$ = 1.15Å [**29**]). The average crystallites size of the materials have been evaluated using peak broadening technique and Scherrer's formula given by $<D_S> = k\lambda/\beta\cos\theta$, where $<D_S>$ is the average particle size, k is the particle shape factor (=0.89), λ is the wavelength of CuK_α radiation (=1.5406Å), β is the full width at half maximum of the XRD peak and θ is the Bragg's diffraction angle of the peak. The as obtained $<D_S>$ are estimated to be mostly of 57,

69 and 76 nm for x = 0, x = 0.10 and x = 0.20 samples, respectively. This result shows that it has no appreciable difference in particle size for all samples.

3.2. Electrical conduction

The variation of resistivity ρ with temperature T of the $(Nd_{1-x}Ce_x)_{0.7}Sr_{0.3}MnO_3$ samples ($0 \leq x \leq 0.20$) was shown in **Fig 2**. The ρ(T) curves reveal that all the samples undergo a metal-semiconductor transition with increasing temperature at T_{MS} = 230, 192 and 186 K for x = 0.00, 0.10 and 0.20, respectively (T_{MS} determined from the maximum of ($d\rho/dT$). It can also be noted that the transition temperature T_{MS} is dependent on Ce concentration. As cerium concentration is increased, the value of maximum resistivity increases and the T_{MS} decreases. Similar behavior has been observed by D. Varshney and al. for $La_{0.7-x}Ce_xCa_{0.3}MnO_3$ **[30].**

In the low temperature ($T < T_{MS}$) metallic behavior, the electrical conduction is generally understood according to the DE theory. In this model, the Mn^{3+}–O–Mn^{4+} coupling produces conduction from the half-filled to the empty eg orbital. As known, the decrease of the resistivity when increasing temperature indicates the presence of semiconductor behavior where the conduction is thermally activated.

The resistivity can be also well fitted, at high temperature ($T > T_{MS}$), by the SPH model

$$\rho(T) = AT \exp\left(\frac{E_{hopp}}{k_B T}\right) \qquad (2)$$

where T is the absolute temperature, k_B is the Boltzmann temperature, A is the pre-exponential factor and E_{hopp} is the activition energy of conduction. The activation energies (E_{hopp}) thus obtained is summarized in **Table 2**. In many cases, the conduction process is related to the electron delocalization phenomenon that is present in this type of material (electron hopping of the eg electron from Mn^{3+} to Mn^{4+} via the O^{2-} orbital), which involves a tendency to form small polarons in the material.

Fig. 3 shows the variation of AC conductance (G_{AC}) with frequency *f* at different temperatures for the $(Nd_{1-x}Ce_x)_{0.7}Sr_{0.3}MnO_3$ compounds (x=0 and x=0.20). These curves are frequency independent in the low frequency region (as shown by the plateau at low frequencies), followed by a sharp increase at high frequencies. In the plateau region, the conductance (G_{DC}) decreases with temperature ($T < T_{MS}$) indicating that the metallic behavior dominates. But the conductance increases with increasing temperature for $T > T_{MS}$ indicating the presence of semiconductor behavior.

The variation of G_{AC} with high frequencies occurs with changes in slope which suggests a superposition of different transport mechanisms in this frequency range. This behavior

indicates that different types of hopping and carrier species are involved in transport. Additionally**,** the AC transport is usually described by the Jonscher power law **[31-33]**:

$$G(\omega) = G_{DC} + A\omega^{n} \quad \textbf{(3)}$$

where G_{DC} is the DC conductance, ω is the angular frequency, A is a pre-exponential factor dependent on temperature and n is the frequency exponent which depends on frequency and temperature. When the frequency is increased, the mean displacement of the charge carriers is reduced and thus the AC conductance of the sample follows the law $G_{AC} = A\omega^{n}$. The frequency dependence of conductance suggests the hopping conduction.

Fig. 4 shows the variation of AC conductance as a function of frequency for all samples at 280 K. It is clear that the conductance decreases with increasing Ce concentration. This behavior is confirmed by the electrical resistivity ρ measurements (**Fig. 2**). The values of G_{DC}, the constant (A) and the exponent (n) for the three samples (x = 0, x=0.10 and x=0.20) are listed in **Table 3**. It can be seen in this table that G_{DC} and n decrease while the A increases when increasing the Ce doping concentration. The variation of the exponent (n) can be expected if the polarizability of involved material depends on the energy barrier for a simple hopping process between two sites **[34].**

The plot of $\ln(G_{DC}T)$ versus 1000/T is shown in **Fig. 5**. At high temperatures, a linear variation was observed, which proves that conductance is dominated by thermally activated hopping of small polaron (SPH) and can be described by Mott and Davis law **[35]:**

$$G_{DC}T = B\exp\left(-\frac{E_{hopp}}{k_B T}\right) \quad \textbf{(4)}$$

Where B is the pre-exponential factor, E_{hopp} is the activation energy of conduction, T is the absolute temperature and K_B is the Boltzmann constant. The activation energies E_{hopp}, as calculated from the slopes (**Fig. 5**), are listed in **Table 2.** It is worth noticing that the energy (E_{hopp}) estimated by both methods yields the same order of magnitude.

3.3. Complex impedance analysis

Impedance spectroscopy is an experimental technique for the characterization of electrical properties of electronic materials. It enables us to separate the real and imaginary components of the electrical parameters and hence provides a true picture of the materials properties.

In general, the complex impedance $Z(\omega)$ under sinusoidal regime can be expressed as:

$$Z(\omega) = Z' - jZ'' \qquad \textbf{(5)}$$

where $Z' = \mathrm{Re}[Z]$ and $Z'' = \mathrm{Im}[Z]$ represent the real and imaginary parts of the impedance $Z(\omega)$, respectively.

Fig.6 shows Nyquist plots (imaginary part of complex impedance Z'' vs real part of complex impedance Z') for $(Nd_{1-x}Ce_x)_{0.7}Sr_{0.3}MnO_3$ (x= 0.20) at several temperatures. The impedance spectrum is characterized by the appearance of some compressed semicircle arcs, which can be well traced with the increase of frequency. The presence of a single semicircular arc indicates that the electrical processes in the material arise basically due to the contribution from bulk material [**36-38**]. The diameter of these semicircles changes with temperature. The center of semicircle making an angle φ with Z'-axis (The angle is between the Z' axis and the line which related the centre of circle with intersection of the semicircular arcs on the real axis) and is temperature-dependent reveals the non-Debye type relaxation process in the material [**39,40**]. These spectra were fitted using Zview software and the best fit is obtained when employing an equivalent circuit formed by a serial association of a grain resistance R_g (bulk resistance) with a resistance R_{gb} (grain-boundary resistance) associated in parallel with constant phase element impedance (Z_{CPE}).

The CPE impedance (Z_{CPE}) is given by the following relation:

$$Z_{CPE} = \frac{1}{A_0(j\omega)^{\alpha}} \qquad \textbf{(6)}$$

Where A_0 indicates the value of capacitance of the CPE element (expressed in Farad units), and α is the factor exponent ($0 < \alpha < 1$).The factor α represents the capacitive nature of the element [**41**]: if α=1, the element is an ideal capacitor and if α=0, it behaves as a frequency independent ohmic resistor. A_0 and α can be temperature dependent.

The values of the bulk (R_g) and the grain boundary (R_{gb}) resistances can be obtained from the intercept of the semicircle and real part of impedance (Z') axis. Accordingly, the intercept of the Z' axis in the right (corresponding to the low frequency) is the sum of R_g and R_{gb}, while the intercept with the Z' axis in the left (corresponding to the high frequency) stands for R_g.

We can reveal from **Fig.6** using **Eq. 6** the real and imaginary components of the impedance related to the equivalent circuit:

$$Z' = Rg + \frac{R_{gb}(1 + R_{gb}A_0\omega^{\alpha}\cos(\frac{\alpha\pi}{2}))}{(1 + R_{gb}A_0\omega^{\alpha}\cos(\frac{\alpha\pi}{2}))^2 + (R_{gb}A_0\omega^{\alpha}\sin(\frac{\alpha\pi}{2}))^2} \quad \textbf{(7)}$$

$$Z'' = \frac{R_{gb}^2A_0\omega^{\alpha}\sin(\frac{\alpha\pi}{2}))}{(1 + R_{gb}A_0\omega^{\alpha}\cos(\frac{\alpha\pi}{2}))^2 + (R_{gb}A_0\omega^{\alpha}\sin(\frac{\alpha\pi}{2}))^2} \quad \textbf{(8)}$$

The parameters (R_g, R_{gb}, A_0 and α) were obtained for each temperature after fitting the data by **Eqs.(7)** and **(8)**. **Fig. 7** shows the variation of the resistance of grains and grain boundaries (inset) of the sample x=0.20 with temperature. The decrease in the values of R_b and R_{gb} (diameters of the semicircular arcs in figure 2) with temperature, above T_{MS}, indicates the presence of thermally activated conduction mechanism in this system which is typical for the semi conductors. Generally two types of thermal activation are responsible for the reduction in resistive properties with temperature **[42, 43]**. In the case of band conduction, carrier density increases with rise in temperature, while in the case of hopping, carrier concentration is determined by the doping level and it is the carrier mobility which is thermally activated. By contrast, the values of grain resistance R_g and the values of grain boundary resistance (R_{gb}) below T_{MS} increase with increasing temperature (metallic behavior). This result is in good agreement with the electrical resistivity.

Fig. 8 shows the variation of real part of impedance ($Z' = \mathrm{Re}[Z]$) with frequency at different temperatures for x=0.20. The impedance value is typically higher in the low-frequency region, and then it decreases gradually with increasing frequency. The decrease in Z' with the increasing frequency may be attributed to the presence of space charge polarization in the material. In fact, this phenomenon has been further verified by observing the coalesced behavior of real part of high frequency impedance for all measured temperatures. Similar behavior at lower frequencies was also observed by Sen et al.[**44**]. We can notice that Z' increases with increasing temperature below T_{MS} (inset of Fig. 8). However, above T_{MS}, it decreases with the increasing of temperature.

Fig. 9 shows the variation of the imaginary part of impedance ($Z'' = \mathrm{Im}[Z]$) with frequency for some representative temperatures. The spectra are characterized by the appearance of peaks, such behavior indicates the presence of relaxation process in the system. Similar behavior has been reported for other manganites and different perovskite systems [**45-47**] and it has been attributed to localized hopping of polarons between lattice sites with a characteristic timescale

[48]. From these peaks we deduce the value of relaxation frequency (*fr)* above T_{MS}, and then we calculate the relaxation time τ using the relation of $\tau = 1/ (2\pi fr)$. It is observed that the value of relaxation time is found to be decreasing with the increase of temperature which represents semiconducting behavior of the sample. This semiconducting nature of the grains in ceramics is believed to be due to the loss of oxygen during high temperature sintering process [**49, 50**]. As a result, the activation energy can be obtained by using the Arrhenius formula $\tau_0 = \tau_0 \exp(\frac{E_{relax}}{k_\beta T})$ **,** τ_0 is the pre-exponential factor, E_{relax} is the activation energy and k_B is the Boltzmann constant. The plot of the relaxation time (τ), as a function of inverse temperature (1000/T), is given in **Fig. 10**. The activation energy (E_{relax}) of the relaxation process and relaxation times at infinite temperature (τ_0) were determined from the slope and intercept, respectively, of the linear least square fits shown as solid lines in **Fig. 10** and the values are listed in **Table 2.** It is observed, from this table, that the activation energy for conduction is greater than relaxation energy .The activation energy for conduction (Ea) is the sum of both the creation of charge carriers and hopping free energy of charge carriers over long distances while the activation energy for relaxation is equal to the migration free energy of charge carriers and their hopping between the adjacent lattice sites. The difference between the conduction and relaxation activation energies may be attributed to the creation of free energy, which shows that the carrier concentration is temperature dependent [51,52].

Conclusion

In summary, we have investigated in this work, the structure and electrical transport properties of $(Nd_{1-x}Ce_x)_{0.7}Sr_{0.3}MnO3$ ($0 \leq x \leq 0.20$) perovskites, using impedance spectroscopy technique over a wide range of temperature and frequency. The X-ray diffraction analysis revealed that all samples exhibit single perovskite with orthorhombic Pnma structure. The electrical investigation shows a metallic semiconductor transition with a metal-like conductivity below and semiconductor-like conductivity above a critical temperature T_{MS}. Electrical conductivity analysis has indicated that conductance can be described by Jonscher universal power law. From the DC conductance study, electronic conduction is found to be dominated by thermally activated hopping of small polarons (SPH), such activation energy was also deduced from the electrical resistivity measured using a conventional four- probe method. Complex impedance analysis indicates that the electrical properties of the material are strongly dependent on temperature and frequency. The

impedance spectrum is characterized by the appearance of semicircle arcs, well modeled in terms of the electrical equivalent circuit. The analysis of the temperature variation of the imaginary-part of the impedance has indicated that the observed relaxation process is thermally activated. From these obtained results, we have deduced the evidence of a hopping mechanism in the conductivity behavior. The activation energies obtained from the conductance is slightly higher than that from time relaxation analyses.

Acknowledgement

This work is supported by the Tunisian National Ministry of Higher Education, Scientific Research and the French Ministry of Higher Education, Scientific Research, within the frame work of collaboration Franco-Tunisian.

References

[1] Y. Tokura (Ed.), For a review, see Colossal-Magnetoresistive Oxides, Gordon & Breach Science Publishers, 1999.

[2] Colossal Magnetoresistance, Charge Ordering and Related Properties of Manganese Oxides, edited by C. N. R. Rao and B. Raveau (World Scientific, Singapore, 1998).

[3] S. Jin, M. McCormack, T.H. Tiefel, R. Ramesh, Thousandfold Change in Resistivity in Magnetoresistive La-Ca-Mn-O Films J. Appl. Phys. 76 (1994) 6929.

[4] J. Yang, Y.Q. Ma, R.L. Zhang, B.C. Zhao, R. Ang, W.H. Song, Y.P. Sun, Structural, transport, and magnetic properties in the Ti-doped manganites $LaMn_1K_xTi_xO_3$ ($0\leq x\leq 0.2$) Solid State Comm. 136 (2005) 268.

[5] C. Zener, Interaction between the d-Shells in the Transition Metals. II. Ferromagnetic Compounds of Manganese with Perovskite Structure, Physical Review 82 (1951) 403

[6]A.J. Millis, P.B. Littlewood, B.I. Shraiman, Double Exchange Alone Does Not Explain the Resistivity of $La_{1-x}Sr_xMnO_3$, Physical Review Letters 74 (1995) 5144.

[7] Y, Kalyana Lakshmi, P, Venugopal Reddy, Influence of sintering temperature and oxygen stoichiometry on electrical transport properties of $La_{0.67}Na_{0.33}MnO_3$ manganite J. Alloys Compd. 470, 67 (2009).

[8] Rao, G.N., Saibal Roy, R.C., Yang, Chen, J.W. Double peak behavior of resistivity curves in Cd doped LaMnO3 perovskite systems, J. Magn. Magn. Mater. 260, 375 (2003).

[9] L.S. Ewe, A.Jemat, K.P.Lim, R.Abd-Shukor, Electrical, magnetoresistance and magnetotransport properties of $Nd_{1-x}Sr_xMnO_3$, Physica B 416 (2013) 17–22.

[10] E. Suard, F. Fauth, C. Martin, A. Maignan, F. Millange, L. Keller, Role of the A-site cations on the magnetic structures and transport properties in the $Nd_{0.7}Ba_{0.3-y}Sr_yMnO_3$ ($0\leq y\leq 0.2$) perovskite, J. Magn. Magn. Mater. 264 (2003) 221–233.

[11] A.J. Millis, Lattice effects in magnetoresistive manganese perovskites, Nature 392 (1998) 147.

[12] I.M. Hodge, M.D. Ingram, A.R. West, Impedance and modulus spectroscopy of polycrystalline solid electrolytes, J. Electroanal. Chem. 74 (1976) 125.

[13] C.Y. Hsu, Hsiung Chou, B.Y. Liao, J.C.A. Huang, Interfacial and quantum well effects on ac magnetotransport of $La_{0.7}Sr_{0.3}MnO_3/La_{1.4}Sr_{1.6}Mn_2O_7$ composites, Appl. Phys. Lett. 89 (2006) 262501.

[14] H.S. Maiti, R.N. Basu, Complex-plane impedance analysis for semiconducting barium titanate, Mater. Res. Bull. 21 (1987) 1107.

[15] N. Sdiri, R. Jemai, M. Bejar, M. Hussein, K. Khirouni, E. Dhahri, S. Mazen, Electrical conductivity and dielectric analysis of the perovskite $La_{0.7}Ca_{0.3-x}K_xMnO_3$ (x=0.00x=0.00, 0.05 and 0.10), Solid State Commun. 148 (2008) 577–581.

[16] M. Nadeem, M.J. Akhtar, M.N. Haque, Increase of grain boundary resistance with time by impedance spectroscopy in $La_{0.50}Ca_{0.50}MnO_{3+\delta}$ at 77 K, Solid State Commun. 145 (2008) 263–266

[17] Yang C P, Chen S S, Dai Q, Guo D H and Wang H, Spin-dependent electroresistance in $Nd_{0.67}Sr_{0.33}MnOy$(y<3.0), Acta. Phys. Sin. 2007, 56 4908

[18] Ying Y, Fan J Y, Pi L, Hong B, Tan S and Zhang Y H,The effect of Ga doping in $Nd_{0.7}Sr_{0.3}MnO_3$ system, Solid State Commun. 2007 , 144 300

[19] G. Venkataiah, V. Prasad, P. Venugopal Reddy, Anomalous variation of magnetoresistance in $Nd_{0.67-y}EuySr_{0.33}Mn0_3$ manganites, Solid State Communications 141 (2007) 73–78

[20] S. Vadnala , S. Asthana , P. Pal , S. Srinath , V. Baranauskas , V.Ralchenko, Influence of Nd Substitution by La in $Nd_{0.7}Sr_{0.3}MnO_3$ on Structural and Transport Properties for Sensing Applications, ISRN Mater Sci. 2013, Vol. 2013.

[21] Langsheng Ling, Jiyu Fan, Li Pi, Shun Tan, Yuheng Zhang, Effect of magnetism and average radius at A-site on T_C in $Nd_{0.6}Ln_{0.1}Sr_{0.3}MnO_3$ (Ln=La, Pr, Gd, Dy) system, Solid State Communications 145 (2008) 11–14

[22] S Kundu and T K Nath J. Phys. Evidence of electronic phase arrest and glassy ferromagnetic behaviour in $Nd_{0.4}Gd_{0.3}/Sr_{0.3}MnO_3$ manganite comparative study between bulk and nanometric samples Condens. Matter. 23 (2011) 356001

[23] The-Long Phan, Zhang, Y. D,Yu, S. C.; Khiem, N. V. Phuc, N. X. J. App. Phys. 111 (2012) Electron-spin-resonance study of Y-doped $Nd_{0.7}Sr_{0.3}MnO_3$ ceramics

[24] K. Padmavathi, G. Venkataiah, P. Venugopal Reddy, Electrical behavior of some rare-earth-doped $Nd_{0.33}Ln_{0.34}Sr_{0.33}MnO_3$ manganites, J. Magn. Magn. Mater. 309 (2007) 237–243

[25] T. Roisnel, J.Rodriguez-Carvajal, Computer program FULLPROF, LLB-LCSIM. May 2003.

[26] C. Krishnamoorthy, K. Sethupathi, V. Sankaranarayanan, R. Nirmala, S.K. Malik, Magnetic and magnetotransport properties of Ce doped nanocrystalline $LaMnO_3$ J. Alloys Compd. 438 (2007) 1–7.

[27] H.M. Rietveld, A profile refinement method for nuclear and magnetic structures, J. Appl. Crystallogr. 2 (1969) 65.

[28] V.M. Goldschmit, Geochemische Verteilungsgesetz der Element 7 (1927) 8.

[29] R.D. Shannon, Revised effective ionic radii and systematic studies of interatomic distances in halides and chalcogenides, Acta Crystallogr., Sect. A 32 (1976) 751.

[30] D. Varshney, I.Mansuri, N.Kaurav, W.Q.Lung, Y.K.Kuo. Influence of Ce doping on electrical and thermal properties of $La_{0.7-x}Ce_xCa_{0.3}MnO_3$ ($0.0 \leq x \leq 0.7$) manganites, J. Magn. Magn. Mater. 324 (2012) 3276–3285

[31] S. Lanfredi, P.S. Saia, R. Lebullenger, A.C. Hernandes, Electric conductivity and relaxation in fluoride, fluorophosphate and phosphate glasses: analysis by impedance spectroscopy, Solid State Ionics 146 (2002) 329.

[32] A.K. Jonscher, Universal Relaxation Law, Chelsea Dielectric Press, London, 1996.

[33] A.K. Jonscher, Dielectric Relaxation in Solids, Chelsea Dielectric Press, London, 1983.

[34] A. Pelaiz-Barranco, M.P. Gutierrez-Amador, A. Huanosta, R. Valenzuela, Phase transitions in ferrimagnetic and ferroelectric ceramics by ac measurements, Appl. Phys. Lett. 73 (1998) 2039-2041.

[35] N.F. Mott, E.A. Davis, Electronic Process in Non-crystalline Materials, Clar- endon Press, Oxford, 1979.

[36] J.T.C. Irvine, D.C. Sinclair, A.R. West, Electroceramics: Characterization by Impedance Spectroscopy , Adv. Mater. 2 (1990) 132–138.

[37] S. Selvasekarapandian, M. Vijaykumar, The ac impedance spectroscopy studies on LiDyO2, Mater. Chem. Phys. 80 (2003) 29–33.

[38] Shrabanee Sen, R.N.P. Choudhary, Mater. Impedance studies of Sr modified $BaZr_{0.05}Ti_{0.95}O_3$ ceramics, Chem. Phys. 87 (2004) 256e263.24]

[39] E. Barsoukov, J. Ross Macdonald, Impedance Spectroscopy Theory, Experiment and Applications, second ed., Wiley Interscience, New York, 2005, p. 14.

[40] U. Intatha, S. Eitssayeam, J. Wang, T. Tunkasiri, Impedance Study of Giant Dielectric Permittivity in $BaFe_{0.5}Nb_{0.5}O_3$ Perovskite, Ceramic Curr. Appl. Phys. 10 (2010) 21.

[41] D.D. Macdonald, Electrochim. Reflections on the history of electrochemical impedance spectroscopy, Acta 51 (2006) 1376.

[42] M. Idrees, M. Nadeem, and M. M. Hassan, Investigation of conduction and relaxation phenomena in $LaFe_{0.9}Ni_{0.1}O_3$ by impedance spectroscopy, J. Phys. D 43, 155401 (2010).

[43] M. Younas, M. Nadeem, M. Atif, and R. Grossinger, Metal-semiconductor transition in NiFe2O4 nanoparticles due to reverse cationic distribution by impedance spectroscopy, J. App. Phys. 109, 093704 (2011).

[44] Sen S and Chaudhary R N P 2004, Impedance studies of Sr modified $BaZr_{0.05}Ti_{0.95}O_3$ ceramics, Mater. Chem. Phys. 87 256

[45] J. L. Cohn, M. Peterca, and J. J. Neumeier, Giant dielectric permittivity of electron-doped manganite thin films, $Ca_{1-x}La_xMnO_3$ ($0 \leq x \leq 0.03$), J. Appl. Phys. **97**, 034102 (2005).

[46] H. Rahmouni, A. Selmi, K. Khirouni, N. Kallel. Chromium effects on the transport properties in $La_{0.7}Sr_{0.3}Mn_{1-x}Cr_xO_3$. J. All. Com. 533. 93– 96(2012)

[47] B. C. Sutar, R. N. P. Choudhary, Piyush R. Das. Dielectric and impedance spectroscopy of $Sr(Bi_{0.5}Nb_{0.5})O_3$ ceramics. Cer. Inter. 40 7791–7798 (2014)

[48] Lily, K. Kumari, K. Prasad, R.N.P. Choudhary, Impedance spectroscopy of $(Na_{0.5}Bi_{0.5})(Zr_{0.25}Ti_{0.75})O_3$ lead-free ceramic, J. Alloys Compd. 453 (2008) 325.

[49] B.P. Das, R.N.P. Choudhary, P.K. Matapattra, Impedance spectroscopy analysis of $(Pb_{0.93}Gd_{0.07})(Sn_{0.45}Ti_{0.55})_{0.9825}O_3$ ferroelectrics, Ind. J. Eng. Mat. Sci. 15 (2008) 152e156.

[50] R. Chourasia, O.P. Shrivastava. Solid State Sciences 14 (2012) 341e348

[51] M. Shah, M. Nadeem, M. Idrees, M. Atif, M. J. Akhtar. Change of conduction mechanism in the impedance of grain boundaries in $Pr_{0.4}Ca_{0.6}MnO_3$. J. Mag. M. Mater. 332 (2013) 61–66

[52] S. Komine, E. Iguchi, Dielectric properties in $LaFe_{0.5}Ga_{0.5}O_3$, J. Phys. Chem. Sol. 68 (2007) 1504.

Tables captions:

Table 1: Refined structural parameters of $(Nd_{1-x}Ce_x)_{0.7}Sr_{0.3}MnO_3$ ($0 \leq x \leq 0.20$) at room temperature. Space group Pnma. V is the cell volume; B_{iso} is the overall isotropic thermal parameter; TM-O the bond lengths between Mn and O and Mn-O-Mn are the bond angles, R_{wp}, R_p and R_F are the agreement factors for the weighted profiles, the profiles and the structure factors; χ^2 is the goodness of fit. The numbers in parentheses are estimated standard deviations to the last significant digit.

Table 2: Activation energy estimated from resistivity, conductance and relaxation plots for $(Nd_{1-x}Ce_x)_{0.7}Sr_{0.3}MnO_3$ (x= 0, 0.10, 0.20) compounds. τ_0 is relaxation time at an infinite temperature.

Table 3: Values of the DC conductance, the constant (A) and the exponent (n), for $(Nd_{1-x}Ce_x)_{0,7}Sr_{0,3}MnO_3$ (x= 0, 0.10, 0.20) compounds, determined at the temperature T=280K.

Figures captions

Figure 1. X-ray diffraction pattern and the corresponding Rietveld refinement of the $(Nd_{1-x}Ce_x)_{0.7}Sr_{0.3}MnO_3$ (x=0 and 0.20) samples.

Figure 2 . The temperature dependence of resistivity ρ for $(Nd_{1-x}Ce_x)_{0.7}Sr_{0.3}MnO_3$ compounds (x = 0, 0.10 and 0.20 content). Solid lines are linear fits to data using SPH model.

Figure 3. Variation of the AC conductance (G_{AC}) as a function of frequency at different temperatures 80–320 K for $(Nd_{1-x}Ce_x)_{0.7}Sr_{0.3}MnO_3$ samples. ((a) x = 0, (b) x = 0.20).

Figure 4. Variation of the AC conductance (G_{AC}) versus frequency *f* of $(Nd_{1-x}Ce_x)_{0.7}Sr_{0.3}MnO_3$ (x = 0, 0.10, 0.20) compounds at the temperature T = 280 K.

Figure 5. Variation of the $\ln(G_{DC}T)$ as a function of (1000/T) for $(Nd_{1-x}Ce_x)_{0.7}Sr_{0.3}MnO_3$ (x = 0, 0.10, 0.20) samples.

Figure 6. Complex impedance plots at given temperatures for $(Nd_{1-x}Ce_x)_{0.7}Sr_{0.3}MnO_3$ (x=0.20) compound.

Figure 7. Variation of Rg and Rgb with temperature for the $(Nd_{1-x}Ce_x)_{0.7}Sr_{0.3}MnO_3$ sample [x = 0.20].

Figure 8 . Variation of real part of the impedance (Z') of the $(Nd_{1-x}Ce_x)_{0.7}Sr_{0.3}MnO_3$ sample (x = 0.20) as a function of frequency for different temperatures.

Figure 9. Variation of imaginary part of the impedance (Z'') of the $(Nd_{1-x}Ce_x)_{0.7}Sr_{0.3}MnO_3$ samples [x = 0.20] as a function of frequency for different temperatures.

Figure 10. Variation of the $\ln(\tau)$ as a function of (1000/T) for the Ce-doped compounds. Solid lines are linear fits to data.

composition		x= 0	x= 0.10	x= 0.20
Space group			*Pnma*	
a (Å)		5.4593(1)	5.4644(2)	5.4674(3)
b(Å)		7.7243(2)	7.7293(3)	7.7183(2)
c(Å)		5.4553(1)	5,4598(1)	5.4690(2)
V ($Å^3$)		230.05(2)	230.60(1)	230.79(3)
(Nd/Ce/Sr)	*x*	0.0276(6)	0.0294(4)	0.0247(3)
At.Positions	*z*	0.0036(5)	0.0038(1)	-0.008(7)
(Nd/Ce/Sr)	$B_{iso}(Å^2)$	1.20(2)	1.12(3)	0.89(4)
(Mn)	$B_{iso}(Å^2)$	0.51(5)	0.82(4)	0.39(1)
O (1)	*x*	0.5012(4)	0.5055(1)	0.4879(2)
At.Positions	*z*	0.0248(2)	0.0295(8)	0.0755(5)
O (1)	$B_{iso}(Å^2)$	0.82(6)	0.83(2)	0.52(2)
O (2)	*x*	0.5012(4)	0.5055(7)	0.4900(6)
At.Positions	*y*	0.4879(2)	0.0295(6)	0.0686(3)
	z	0.24(6)	0.12(2)	-0.29(1)
O (2)	$B_{iso}(Å^2)$	1.47(3)	1.68(3)	1.30(2)
$\langle d_{Mn-O1} \rangle$ *(Å)*		1.936(1)	1.940(2)	1.982(9)
$\langle \theta_{Mn-O1-Mn} \rangle$ *(°)*		172.059(3)	169.80(2)	158.545(1)
$\langle d_{Mn-O2} \rangle$ *(Å)*		1.8237(2)	1.720(1)	1.67(4)
$\langle \theta_{Mn-O2-Mn} \rangle$ *(°)*		154.475(4)	156.4 (3)	167.313(3)
$\langle d_{Mn-O} \rangle$ *(Å)*		1.8615	1.830	1.826
$\langle \theta_{Mn-O-Mn} \rangle$ *(°)*		163.280	163.10	162.929

t_G	0.9014	0.9022	0.9030
$<r_A>$	1.2071	1.2089	1.2108
R_p (%)	4.77	5.65	5.56
R_{wp} (%)	6.37	7.86	7.94
R_F (%)	4.83	5.06	6.67
χ^2 (%)	2.71	3.97	3.73

Table 1:

Table 2

composition	Resistivity analysis	Conductance analysis	Relaxation analysis	
	E_{hopp} (meV)	E_{hopp} (meV)	E_{relax} (meV)	Relaxation time (s) τ_0
x=0	81	80	61	7.22 E-7
x=0.10	90	88	65	6.75 E-7
x=0.20	93	94	75	1.85 E-6

Table 3:

x	G_{DC}	A	exponent n
0	6.85E-2	4.715E-12	1.94
0.10	6.15E-2	3.043E-13	1.88
0.20	8.20E-3	1.043E-13	1.79

Fig. 1.

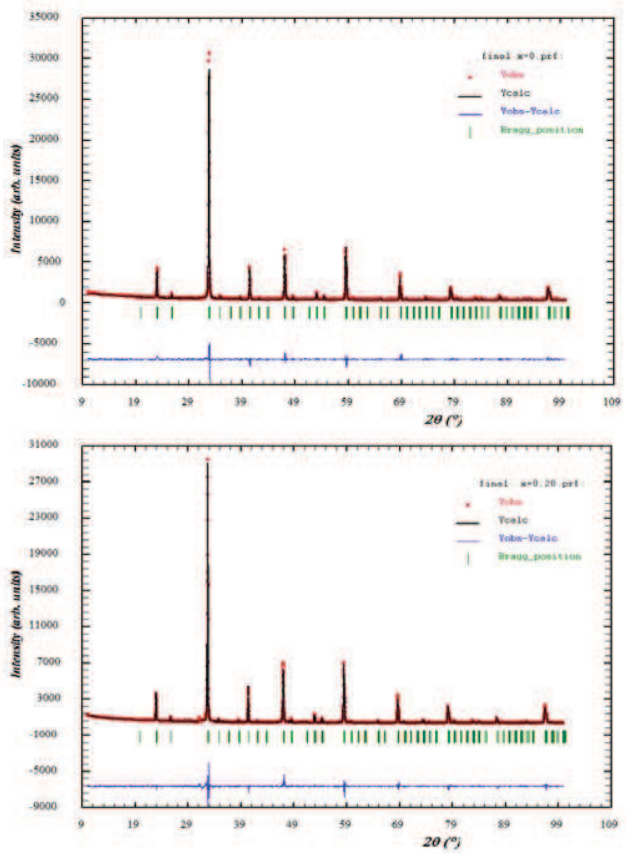

Fig. 2.

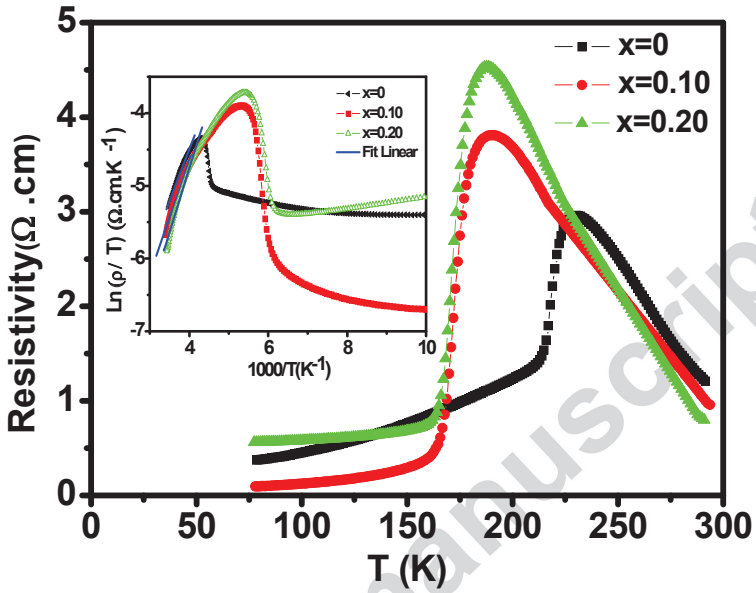

Fig. 3.

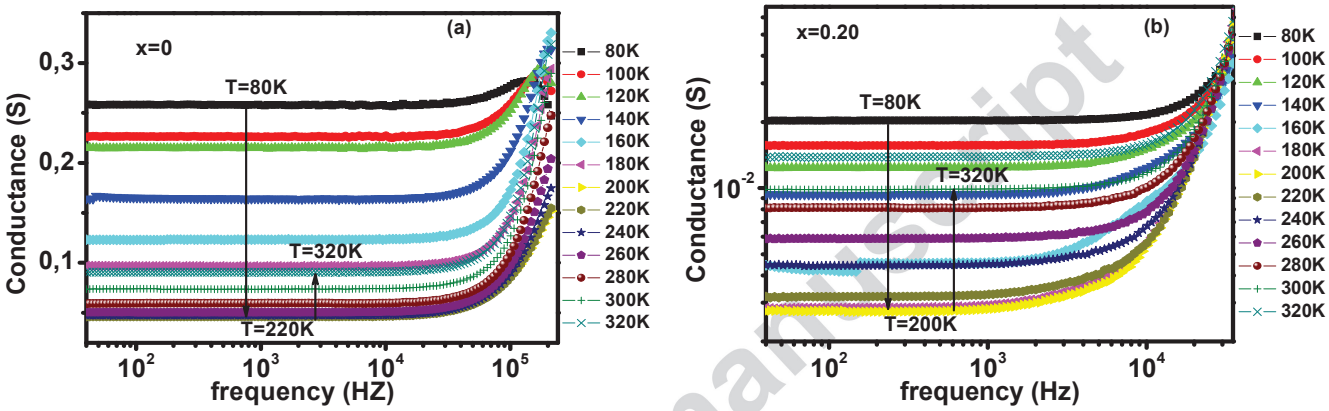

Fig. 4.

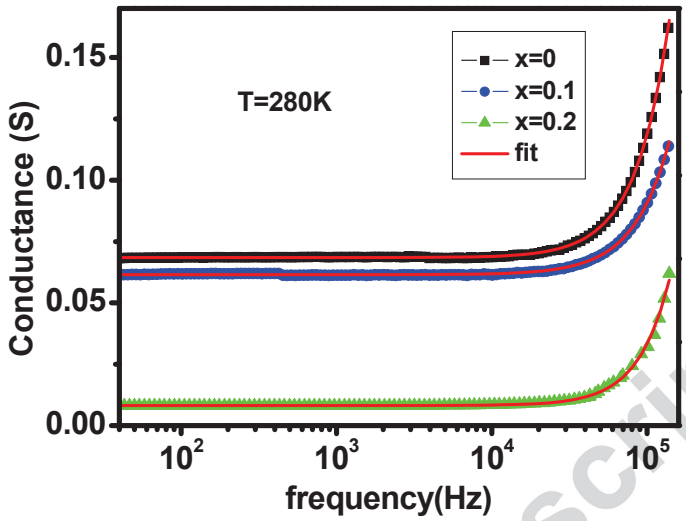

Fig. 5.

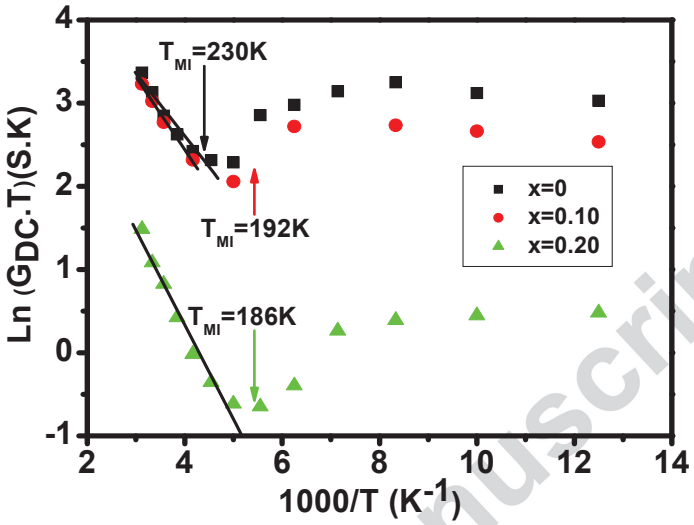

Fig. 6.

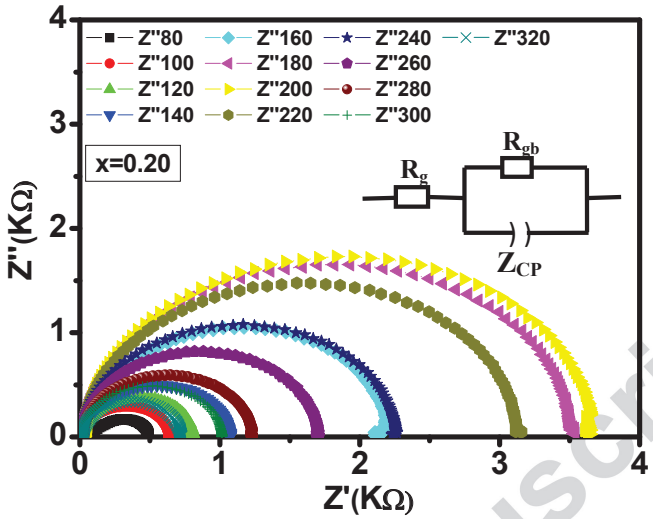

Fig. 7.

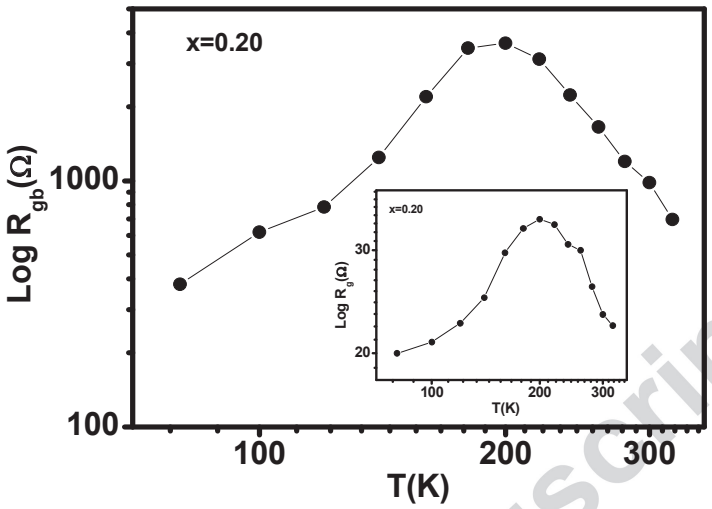

Fig. 8.

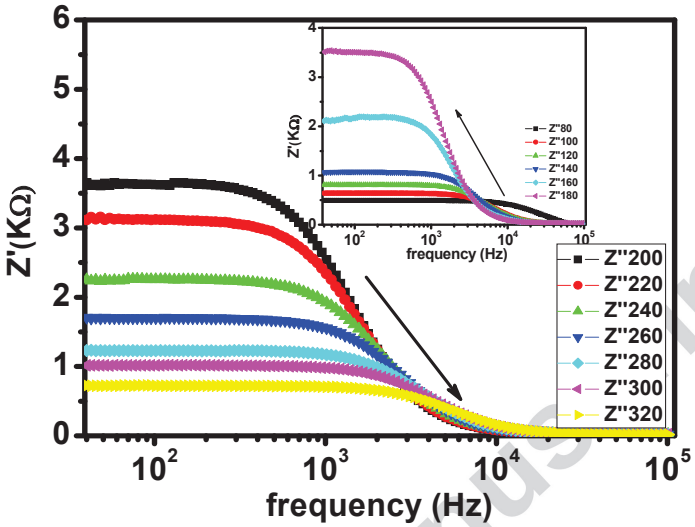

Fig. 9.

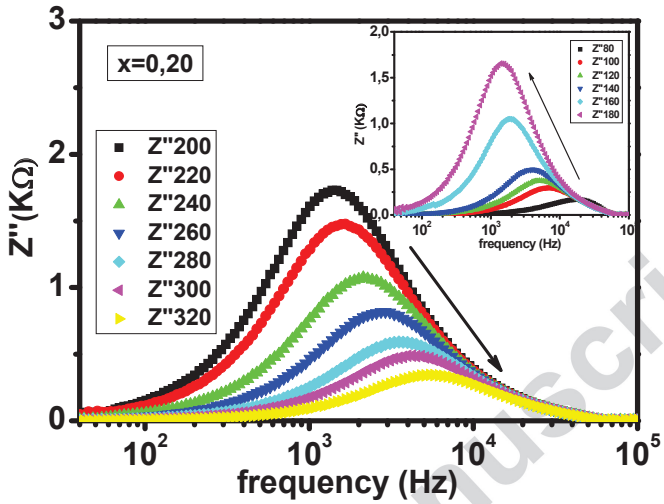

Fig. 10.